The Indo-Pacific Maritime Continent Barrier Effect on MJO Prediction

S. ABHIK,[a] HARRY H. HENDON,[a,b] AND CHIDONG ZHANG[c]

[a] *Bureau of Meteorology, Melbourne, Victoria, Australia*
[b] *School of Earth, Atmosphere and Environment, Monash University, Clayton, Victoria, Australia*
[c] *NOAA/Pacific Marine Environmental Laboratory, Seattle, Washington*

(Manuscript received 6 January 2022, in final form 26 September 2022)

ABSTRACT: The Madden–Julian oscillation (MJO) is often observed to weaken or sometimes completely decay as its convective anomaly moves from the Indian Ocean over to the Maritime Continent (MC), which is known as the MC barrier effect on the MJO. This barrier effect is often exaggerated in numerical models. Using 23 years of the retrospective intraseasonal forecast from two coupled model systems with useful MJO prediction skills, we show that the predictive skill of the real-time multivariate MJO (RMM) index for the continuously propagating MJO events across the MC region is higher than for the blocked MJO events. The greater prediction skill is not related to the higher initial RMM amplitude for the continuous MJO events. Rather the higher skill arises from the more persistent behavior of the propagating MJO events as the convective anomaly moves through the MC region into the western Pacific. The potential predictability is similar for both types of MJO events, suggesting the forecast models hardly differentiate the two types of MJO events in prediction; they only maintain higher RMM magnitudes of the continuously propagating events. The global reanalysis dataset indicates that the blocked events are often associated with persistent higher surface pressures over colder sea surface temperatures in the central Pacific, suggesting the large-scale environment plays a role in promoting or inhibiting the MJO propagation across the MC region. Caveats in the models to reproduce the observed MJO events are also discussed.

KEYWORDS: Maritime Continent; Atmosphere–ocean interaction; Madden–Julian oscillation; Forecast verification/skill; Subseasonal variability; Tropical variability

1. Introduction

The Madden–Julian oscillation (MJO; Madden and Julian 1971, 1972) is a tropical planetary-scale, eastward-propagating, convection–circulation coupled perturbation. MJO convective signals are largely confined to the Indo-Pacific warm pool, extending from the western Indian Ocean to the western Pacific, while its upper-level circulation anomalies extend globally near the equator. Closer inspections of its convective signals reveal two main centers of enhanced variance associated with the MJO, one in the Indian Ocean and the other in the western Pacific. The behavior of the convective anomalies as they leave the Indian Ocean and encounter the Indo-Pacific Maritime Continent (MC) region is often erratic: the convective anomalies weaken, slow down, and sometimes completely dissipate before emerging over the western Pacific (Kim et al. 2014; Zhang and Ling 2017). Because of this, the MC region is referred to as a barrier to the MJO propagation (e.g., Zhang and Ling 2017). The MC "barrier effect" is often exaggerated in numerical prediction models (e.g., Vitart and Molteni 2010), and consequently, it is considered a predictability barrier for the MJO (Kim et al. 2016). To date, there is a lack of full understanding of the mechanisms for the MC barrier effect and the MJO prediction barrier. A comprehensive understanding of the role of the barrier effect on the MJO prediction would be of considerable value in revealing the key physical processes and improving the forecast capability.

A few mechanisms for the barrier effect of the MC region on the MJO have been proposed. They include reduced air–sea surface fluxes due to the presence of the islands (Maloney and Sobel 2004; Sobel et al. 2010), topographic distortion of the planetary-scale low-level circulation that is fundamental to the existence of the MJO (Hsu and Lee 2005; Inness and Slingo 2006; Wu and Hsu 2009; Tan et al. 2020), modulation of moisture distribution by the large-scale circulations (Kim et al. 2014; Feng et al. 2015; DeMott et al. 2018), and the strong diurnal cycle in convection over the islands that might inhibit the large-scale organization of the MJO (Houze et al. 1981; Mori et al. 2004; Yamanaka 2016). When MJO convection moves across the MC region, the persistent diurnal cycle over the islands could weaken the MJO convection by interrupting the cloud–radiation feedback (Neale and Slingo 2003; Hagos et al. 2016; Majda and Yang 2016), which is thought to be one of the primary drivers of the eastward-propagating intraseasonal convective anomalies (Hu and Randall 1994, 1995; Sobel and Maloney 2013). Zhang and Ling (2017) suggested stronger lower-level zonal moisture flux convergence and higher sea surface temperature (SST) around the MC region may weaken the barrier effect and promote MJO

Denotes content that is immediately available upon publication as open access.

Supplemental information related to this paper is available at the Journals Online website: https://doi.org/10.1175/JCLI-D-22-0010.s1.

Abhik's current affiliation: School of Earth, Atmosphere and Environment, Monash University, Clayton, Victoria, Australia.

Corresponding author: S. Abhik, abhik.climate@gmail.com

DOI: 10.1175/JCLI-D-22-0010.1

propagation across the MC islands. The zonal overturning circulation of strong MJOs over the Indian Ocean is composed of low-level easterly wind anomalies to the east as a result of the Kelvin wave response to the east of MJO convection (Kim et al. 2014). Besides, a westward-tilted low-level moistening over the MC can lead to premoistening ahead of the main MJO convective center (Johnson et al. 1999), hence setting up a strong vanguard of precipitation over the islands (Rowe and Houze 2015; Ruppert and Johnson 2015). On the other hand, Chen and Wang (2018) suggested that the leading suppressed convection of the Indian Ocean MJO convection along with a front Walker cell over the MC and the western Pacific could help the MJO propagate through the MC. The MJO events that are not able to transit the MC region do not possess a well-defined zonal overturning circulation with premoistening over the MC (Ling et al. 2019).

The MJO continues to be a great challenge for the current GCMs (Weaver et al. 2011; Kim et al. 2016; Ahn et al. 2020), and consequently, the predictive skill for MJO remains limited to 4 weeks (e.g., Vitart et al. 2017), even though its potential predictability is more than 5 weeks (Waliser et al. 2003). The systematic eastward propagation and eastward extent of the MJO are not realistically represented in most of the participating GCMs in the MJO Task Force (MJOTF) and the GEWEX Atmospheric System Study (GASS) modeling experiments (Jiang et al. 2015; Ling et al. 2019). Results have suggested that the models with a wetter lower troposphere over the MC and stronger meridional moisture gradient could better reproduce MJO propagation across the MC region (Jiang 2017). Additionally, a realistic representation of the precipitation distribution over the complex land–ocean systems of the MC region is also found to be critical for the MJO propagation across the MC (Peatman et al. 2014; Baranowski et al. 2019). Although the barrier effect is highlighted in many studies, its impact on the capability to forecast the MJO is still uncertain (Kim et al. 2016).

The objective of this study is to assess the barrier effect of the MC on the MJO prediction skills in initialized multiweek predictions of coupled models. MJO events are identified in advance as "continuously propagating" across the MC region or "blocked" by the MC region based on the observed behavior. We use two forecast systems that have reasonable MJO prediction skills to about 3–4-week lead time (Marshall and Hendon 2019) and are considered among the leading S2S models for MJO prediction (Vitart et al. 2017). Because the coupled models drift and systematic error develops in the depiction of the MJO at the long lead time, we mainly focus on differences in predictive skill for "blocked" and "continuous" MJOs at lead times ~2–4 weeks. The models, data, and methodology used are introduced in section 2, results are discussed in section 3, and concluding remarks are made in section 4.

2. Model, data, and methodology

The Predictive Ocean Atmosphere Model for Australia (POAMA), version 2 (Hudson et al. 2013), was the ocean–atmosphere coupled prediction system used operationally for seasonal prediction at the Australian Bureau of Meteorology (BOM) during 2011–2018. The atmospheric component of POAMA has a horizontal resolution of ~250 km and 17 vertical levels with the model top at ~9 hPa. The ocean model is based on Geophysical Fluid Dynamics Laboratory (GFDL) MOM2 and has a resolution of 2° longitude × 0.5° latitude at the equator with 25 vertical levels. To produce hindcasts for the period 1980–2016, the model's atmosphere is initialized by strongly nudging to ERA-40 (Hudson et al. 2011) and ocean initial conditions are provided by the POAMA Ensemble Ocean Data Assimilation System (PEODAS; Yin et al. 2011), which uses an ensemble optimum interpolation of available subsurface temperature and salinity observations to produce an ocean analysis every 24 h. An ensemble of ocean–atmosphere initial conditions is produced using a coupled breeding method (Hudson et al. 2011). POAMA's performance for predicting the MJO is well documented (e.g., Marshall et al. 2011), and in this study, we use the reforecasts initialized on day 1, 6, 11, 16, 21, and 26 of each month between December and March (DJFM) during 1990–2012. Reforecasts extend to a 9-month lead time, but we concentrate on MJO behaviors in the first month. Model uncertainty is addressed by running three versions of the model, two of which use slightly different moist physics and one version is flux corrected (Hudson et al. 2013). A 33-member ensemble forecast from three versions of POAMA 2.4 (e24a, e24b, and e24c) is available. But we consider 11-member forecasts from the original version of the model (e24c) to be compatible with the other model used in this study.

We also analyze the prediction of Australian Community Climate and Earth-System Simulator Seasonal Prediction System, version 1 (ACCESS-S1; Hudson et al. 2017). It replaced the POAMA operational seasonal forecasting system at the BOM in 2018 and was operationally used for subseasonal-to-seasonal prediction at the BOM during 2018–2021. ACCESS-S1 is based on the UKMO Global Seasonal Forecast System, version 5, using the global coupled model configuration 2 (MacLachlan et al. 2015). The horizontal resolution of the atmospheric model is ~60 km, and it has 85 vertical levels with a well-resolved stratosphere (35 levels above 18 km; Walters et al. 2017). The ocean model, based on Nucleus for European Modeling of the Ocean (NEMO ORCA25; Megann et al. 2014), has a 25-km horizontal resolution and 70 vertical levels (~1-m resolution in the top 10 m). For the hindcasts used here, the atmospheric initial conditions are derived by interpolating European Centre for Medium-Range Weather Forecasts (ECMWF) interim reanalysis (ERA-Interim, hereafter ERA-I; Dee et al. 2011) directly onto the model grid. The ocean initial conditions are obtained from the Forecast Ocean Assimilation Model analyses at the UKMO (Blockley et al. 2014), which is 3D variational assimilation of available temperature, salinity, and sea level observations. Reforecasts are available from 1, 9, 17, and 25 of each month during DJFM 1990–2012. An 11-member ensemble is produced by perturbing the atmospheric initial conditions (Hudson et al. 2017).

Blocked and continuous MJO events are identified following Ling et al. (2014), which track the intraseasonally filtered eastward-propagating positive precipitation anomalies near the equator that has the characteristics of the MJO. Their

method identifies starting and ending longitudes, and the dates of the positive precipitation anomalies. We focus on the MJO cases that begin in the Indian Ocean (the bulk of the events) and refer to the blocked MJOs around the MC islands as MJO-B, while those exhibiting continuing eastward propagation of the positive precipitation anomaly across the MC region into the western Pacific are defined as MJO-C. It is noteworthy that the MJO-B events are fundamentally different from "standing" MJOs defined in Wang et al. (2019). The standing MJOs, unlike MJO-B events, are confined to the Indian Ocean and do not interact with the MC islands.

For the extended austral summer season (DJFM) 1990–2012, which is the common period for the hindcasts from POAMA and ACCESS-S1, 13 MJO-B and 14 MJO-C events that originate in the Indian Ocean are identified. We define "day 0" when the MJO positive precipitation anomaly is in the 85°–95°E longitude band. This region is downstream from that where the typical MJO events initiate and is just upstream of the MC region. However, our results are not sensitive to the chosen longitude band. We examine the behavior of the observed MJO events from day −10 to day +29. To evaluate the predicted MJO events, we use the reforecasts initialized within ±3 days of day 0 and analyze up to 30 lead days. In this study, we select 14 (22) MJO-B and 21 (26) MJO-C start dates in ACCESS-S1 (POAMA). As both models have different forecast initialization frequencies in a calendar month, the number of start dates differs only, but the predictions of the same observed MJO events are considered.

We use daily surface temperature, mean sea level pressure (MSLP), and 37 standard pressure level (available between 1 and 1000 hPa) zonal wind, vertical pressure velocity, and specific humidity analyses from ERA-I, which are provided globally on a 0.75° spatial resolution. We also monitor the MJO using the real-time multivariate MJO (RMM) index (Wheeler and Hendon 2004). The observed RMM index is derived by projecting equatorially averaged (15°S–15°N) anomalies of daily top-of-the-atmosphere outgoing longwave radiation (OLR; Liebmann and Smith 1996) and zonal winds at 850 (u850) and 200 hPa (u200) from National Centers for Environmental Prediction (NCEP) reanalysis (Kalnay et al. 1996) onto the leading pair of observed empirical orthogonal functions provided by Wheeler and Hendon (2004). This provides a pair of temporal components commonly referred to as RMM_1 and RMM_2, which are normalized by their own standard deviation. They are temporally uncorrelated at zero lag but strongly correlated at a lag of about 1/4 cycle of the MJO (i.e., about 12 days). The predicted RMM index for each ensemble member is computed by projecting the predicted equatorially averaged OLR and zonal wind anomalies onto the same pair of observed empirical orthogonal functions. The predicted anomalies are formed by removing the lead time–and start time–dependent model climatology for 1990–2012. Before projecting the forecast anomalies onto the observed eigenvectors, the previous 120-day mean, which is a combination of observed and forecast data, is subtracted from each field following the approach of Rashid et al. (2011). The daily RMM amplitude (observed and predicted) is defined as

$$|\mathrm{RMM}(t)| = \sqrt{\mathrm{RMM}_1^2(t) + \mathrm{RMM}_2^2(t)}.$$

For dynamical model prediction skill comparison, we also use the statistical model developed by Maharaj and Wheeler (2005), referred to as the vector autoregressive (VAR) model. The VAR scheme for austral summer is

$$\mathrm{RMM}_1(t+1) = 0.9696 \times \mathrm{RMM}_1(t) - 0.1111 \times \mathrm{RMM}_2(t),$$
$$\mathrm{RMM}_2(t+1) = 0.1258 \times \mathrm{RMM}_1(t) + 0.9626 \times \mathrm{RMM}_2(t).$$

Additionally, the OLR-based MJO index (OMI; Kiladis et al. 2014) is used to examine the MJO propagation. It is formed similarly to the RMM index, providing a pair of temporal components, but uses only bandpass-filtered OLR as input. The OMI provides complementary information to the RMM index as it is focused only on the convective component of the MJO. OMI results are generally similar to those using the RMM index and are shown in the supplementary sections.

3. Results

a. Observed MJO events

We first examine the observed rainfall, OLR, and RMM amplitude on day 0 for MJO-B and MJO-C events. The rainfall and OLR anomalies are averaged over 15°S–15°N, 90°–100°E for 14 MJO-C and 13 MJO-B events on day 0. We test the significance of the anomalies and RMM amplitude using a permutation resampling approach with a null hypothesis of no difference between MJO-C and MJO-B. We randomly select 14 and 13 cases from MJO-C and MJO-B pools with replacement and recompute the averaged anomalies and RMM amplitude 5000 times. The 5% level of significance of the null hypothesis is obtained from the 2.5th and 97.5th percentiles of the resampled values. The observed values for MJO-B and MJO-C and 95% confidence interval about the null hypothesis are shown in Table 1 for rainfall, OLR, and RMM amplitude. If the confidence intervals do not overlap, then the values are considered to be significantly different at a 5% level. Although average rainfall and OLR anomalies over the eastern Indian Ocean are higher for MJO-C, the values are not significantly different at the $p = 5\%$ level. Consistent with

TABLE 1. The rainfall, OLR anomalies averaged over the eastern Indian Ocean (15°S–15°N, 90°–100°E), and RMM amplitudes on day 0 for MJO-B and MJO-C events. The 95% confidence intervals about the null hypothesis of no difference are mentioned in parentheses. The difference significant at a 5% level is shown in boldface.

	MJO-B	MJO-C
Rainfall (mm day^{-1})	0.81	1.87
	(−1.82, 1.69)	(0.058, 2.12)
OLR (W m^{-2})	−10.3	−17.55
	(−15.83, 0.33)	(−26.92, −3.76)
RMM amplitude	**1.06**	**1.77**
	(0.73, 1.4)	(1.42, 1.92)

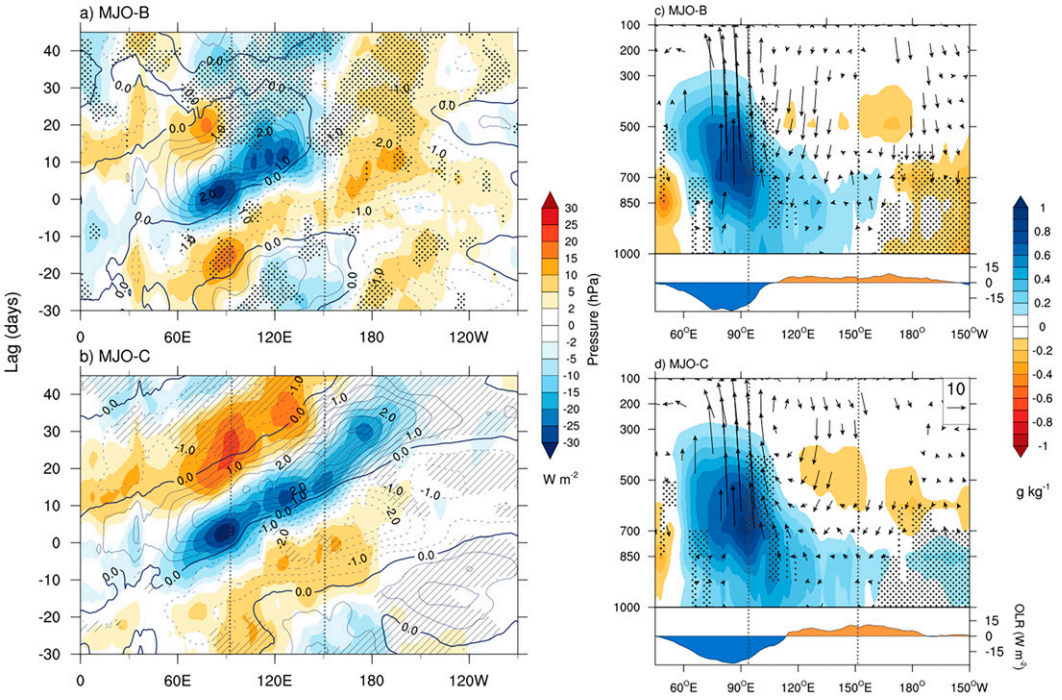

FIG. 1. (a),(b) Equatorially averaged (10°S–10°N) observed OLR (shaded) and ERA-Interim 850-hPa zonal wind (contours) anomalies composited for (a) MJO-B and (b) MJO-C events during December–March 1990–2012. Contour interval is 0.5 m s^{-1}. Stippling (hatching) indicates where the difference in the composited OLR (U850) anomalies are significant at the 5% level. A 7-day running mean is applied to the composited fields to remove high-frequency noise. (c),(d) (top) Longitude–pressure cross section of the 10°S–10°N ERA-Interim specific humidity (shaded, g kg^{-1}), zonal and vertical wind (vectors) anomalies for MJO-B and MJO-C events at day 0. Stippling indicates the significant difference in moisture anomalies at the 5% level, while the vectors are only shown where the wind difference is significant at the 5% level. The vector scale (in m s^{-1}) is in the upper right of (d). The vertical velocity has been multiplied by 1000 for display. (c),(d) (bottom)The 10°S–10°N-averaged OLR anomalies are displayed to represent the location of the MJO convection. The gray vertical dotted lines in each panel represent the approximate location of the Maritime Continent islands.

previous studies (e.g., Kim et al. 2014; Zhang and Ling 2017), the OLR and rainfall amplitudes of MJO-C and MJO-B suggest that the local convective anomalies for both types of MJO events are not distinctly different over the eastern Indian Ocean. However, the RMM amplitude is about 67% stronger for MJO-C than for MJO-B and this difference is significant at $p = 5\%$. These results suggest two possibilities: first, convective heating is more effective in forcing the circulation for MJO-C than MJO-B. Second, the stronger circulation of MJO-C has nothing to do with local convection over the eastern Indian Ocean. Both possibilities beg further investigations.

The barrier effect on observed MJO propagation is examined by a lag composite analysis about day 0 for the OLR and 850-hPa zonal wind anomalies. Figures 1a and 1b show the lag–longitude plot of equatorially averaged (10°S–10°N) OLR and 850-hPa zonal wind anomalies composited for all MJO-B and MJO-C events. The MJO-C convective and zonal wind anomalies propagate coherently and continuously from the Indian Ocean into the western Pacific across the MC. As expected, the low-level zonal wind anomalies show a near-quadrature relationship with the OLR anomalies, with westerly anomalies trailing behind enhanced convection (negative OLR anomalies). In contrast, MJO-B convection propagation is confined to the west of the MC, while there is some appearance of rapid eastward propagation of the zonal wind anomalies to the east of the MC region. This rapid eastward propagation in zonal wind into the central Pacific is consistent with the notion that the zonal wind anomaly typically decouples from the MJO convection once it diminishes over the cold waters of the central Pacific (e.g., Hendon and Salby 1994) and so the propagation speeds up. Similar decoupled zonal wind anomalies are evident for MJO-B events, but the associated convective anomaly is terminated by the MC region rather than by the cold waters of the central Pacific.

Figures 1c and 1d show moisture and zonal vertical wind anomalies along the equator (10°S–10°N) for MJO-B and MJO-C at day 0. The equatorial OLR is shown at the bottom of each panel to identify the location of the corresponding center of MJO convection. The vertical structure of the specific humidity and wind are largely similar for MJO-B and MJO-C. The positive moisture anomalies extend slightly broader for MJO-C. The most striking difference between these two types of MJO events is the presence of subsidence

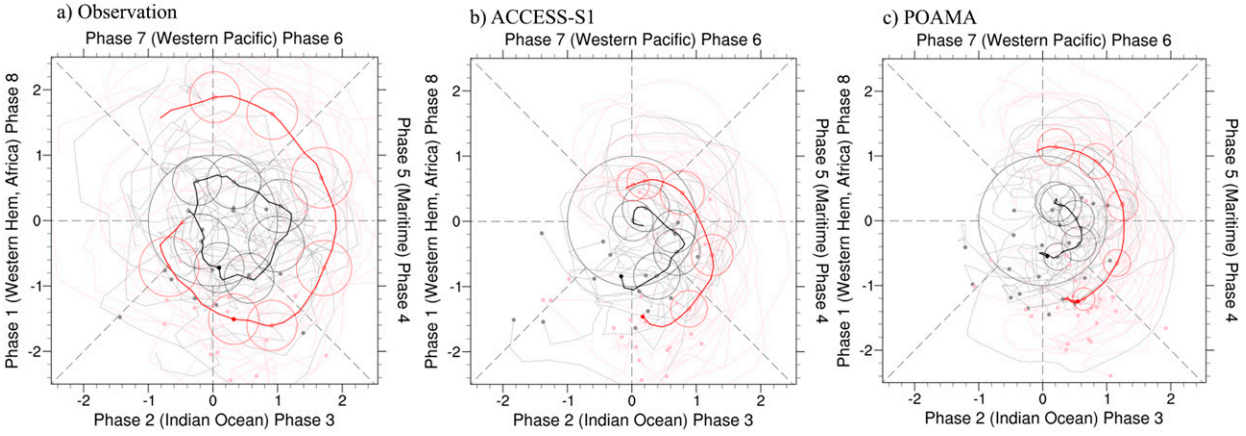

FIG. 2. RMM phase-space diagram for MJO-B (black) and MJO-C (red) events during December–March 1990–2012 for (a) observations and predictions from (b) ACCESS-S1 and (c) POAMA. Individual events in observation and 11-member ensemble-mean predictions are shown using thin curves, and the mean RMM of all cases and ensemble members is shown using thick curves. The observed RMMs are shown from lag −10 to lag +29, with the heavy filled dot indicating day 0. Lighter dots are drawn at a 5-day interval. The predictions run from day 0 through day +29. The unfilled circles every 5 days exhibit the 95% confidence interval of the composited RMM index (see text for details).

in the mid–lower troposphere to the east of 150°E for MJO-B, which is much weaker or absent for MJO-C. The suppressed convection in the upper–midtroposphere and increased moisture in the boundary tend to increase the column-integrated moist static energy (MSE) and likely facilitate eastward propagation of MJO-C (e.g., Sobel et al. 2014). The subsidence is semipersistent (not shown) to the east of the MC and so may act as a barrier to the MJO convection across the archipelago region through the modification of the Walker circulation over the Pacific. Presumably, this persistent subsidence is boundary forced (e.g., as a result of cold SST anomalies), which we explore further in section 3d. For MJO-B, low-level moisture anomalies are negative, possibly related to the strong subsidence near the date line where convection is suppressed (Fig. 1b).

The evolution and strength of the two types of MJO events are further quantified in the RMM phase-space (Wheeler and Hendon 2004). In the RMM phase-space, MJO lifespan is divided into eight phases and its amplitude is considered strong when $|\mathrm{RMM}(t)| > 1$. The propagation characteristics of observed MJO-B and MJO-C events during DJFM and their corresponding mean RMM amplitudes are presented in the phase-space diagram in Fig. 2a. We show the evolution of the MJO events from days −10 to +29. The 95% confidence circles are drawn at every 5-day interval, which are based on the mean standard error of RMM_1 and RMM_2 on that day. Around day −10, both types of MJO events appear over the western Indian Ocean (phases 1 or 2) with weak RMM amplitudes and eventually propagate into the eastern Indian Ocean (phase 3) by day 0 (marked by filled dots in Fig. 2). By this time, MJO-C events grow stronger and maintain their amplitude across the subsequent phases out to day +29. In contrast, MJO-B events briefly become strong only over the eastern Indian Ocean, and they are eventually heavily damped across the MC. The difference in amplitude between MJO-C and MJO-B events is statistically significant at a 5% level beyond day +15. The OMI-based phase-space diagram (Fig. S1 in the online supplemental material) also shows a similar difference.

b. *Predicted MJO events*

The RMM phase-space diagrams of predicted MJO-B and MJO-C (initialized around day 0) in ACCESS-S1 (Fig. 2b) and POAMA (Fig. 2c) also apparently indicate that both models can differentiate these two types of MJO events in their forecasts, with the amplitude of the mean RMM remaining stronger for a longer period and showing more continuous propagation around the phase-space for the MJO-C events than the MJO-B events. Although the predicted MJO-C events in ACCESS-S1 are considerably weaker than that observed beyond the 15-day lead, they steadily propagate into phase 5, maintaining reasonably large amplitude, while the predicted MJO-B are consistently weaker at all lead times. POAMA also predicts the observed differences between MJO-B and MJO-C. The predicted MJO-C events in POAMA propagate into the western Pacific by maintaining a reasonably large amplitude. For both types of events, abundant variability is predicted among the individual MJO events. For instance, a few predicted MJO-B events appear to make it into the western Pacific with large amplitude in both models. Overall, the barrier effect is more evident in ACCESS-S1 for both MJO-B and MJO-C events, with predicted RMM amplitudes of MJO-C quickly reduced over the MC region. However, this exaggerated barrier effect is less apparent in POAMA.

To quantify the predictive skill of these two types of MJO events, we next assess the bivariate correlation and root-mean-square error (RMSE) using the ensemble-mean prediction of the RMM index (Rashid et al. 2011). The bivariate correlation and normalized RMSE (normalized by observed bivariate standard deviation) of ACCESS-S1 forecast are computed for lead times out to 40 days and are shown in Fig. 3. The RMM forecast

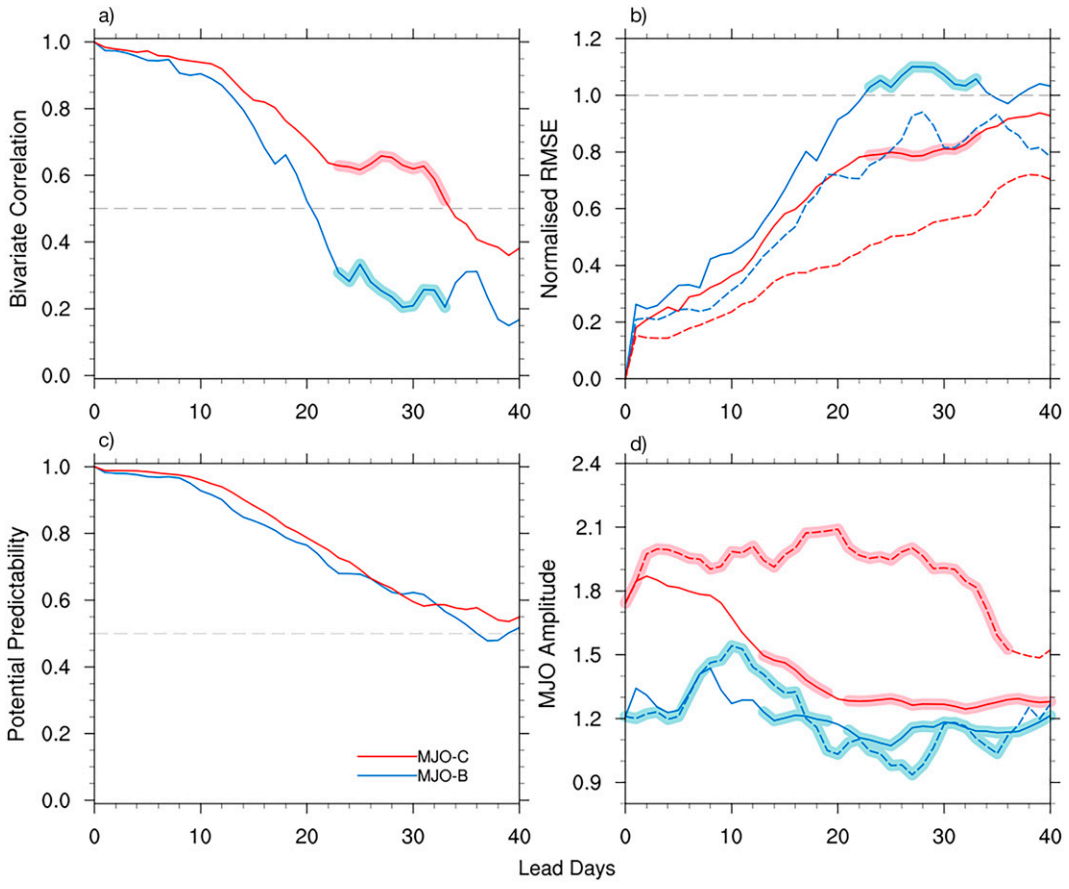

FIG. 3. (a) Bivariate correlation, (b) normalized root-mean-square error (solid curves) and ensemble spread (dashed curves), (c) potential predictability (see text), and (d) mean RMM amplitude (computed for each ensemble member first and then averaged over all ensemble members and cases) from ACCESS-S1 forecast for the MJO-B (blue) and MJO-C (red) events for start times near day 0 during December–March 1990–2012. Shading in (a), (b), and (d) indicates where the difference in bivariate correlation, RMSE, and RMM amplitude is significant at the 5% level. In (d), the solid curves are based on the predictions and the dashed curves represent observed RMM amplitude.

is commonly considered to be "skillful" with correlation > 0.5 (Murphy and Epstein 1989) and normalized RMSE (normalized by observed standard deviation of RMMs) <1. The ACCESS-S1 forecast skill is systematically higher for MJO-C, achieving skillful forecast out to 33 days compared to 20 days for MJO-B. Statistically significant difference in the skills is highlighted by thickening the curves. The significance is estimated using a t test assuming a null hypothesis of no difference, and the effective sample size is derived by considering the lead time–dependent correlation of the ensemble members (Bretherton et al. 1999), following Abhik and Hendon (2019). The prediction skill of the MJO-C events is significantly higher than that of MJO-B events at a 5% level beyond the 25-day lead, indicating substantially better deterministic prediction of individual MJO-C events.

To estimate the uncertainties in the ensemble prediction, the normalized ensemble-mean error (defined as RMSE of ensemble mean) and ensemble spread are computed. Ideally, for a large sample of the forecast, the ensemble spread should be equal to the ensemble-mean error for a well-calibrated forecast (e.g., Weisheimer et al. 2011). The normalized RMSE grows faster for MJO-B and exceeds the threshold of 1 at about a 20-day lead (Fig. 3b). MJO-C has a relatively smaller RMSE at any given lead time, and the error growth rate is slower than MJO-B, largely consistent with higher bivariate correlation. The RMSE is greater than ensemble spread for both MJO cases at all lead times, suggesting the ensemble prediction system is underdispersive. However, no considerable difference is noted in potential predictability for these two types of MJO events, calculated following Rowell (1998). For both types of MJO events, the predictability, measured as the ratio of the ensemble-mean variance to the total ensemble variance, extends beyond 40 days (Fig. 3c). This lack of difference in potential predictability suggests that the difference in model prediction skills between MJO-B and MJO-C events does not come from the barrier effect. Rather, any difference in skill may appear due to differences in initial amplitude. This is explored further below.

The shortcoming of the model is also reflected in the mean of the ensemble and all the cases' RMM amplitudes at longer lead days. In observations and forecasts, the initial RMM

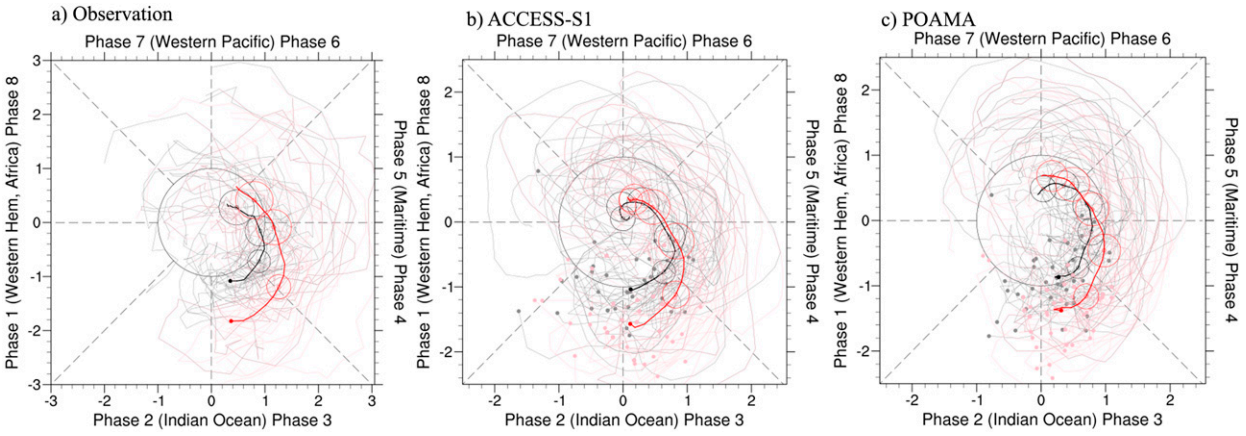

FIG. 4. RMM phase-space diagram for weak (black) and strong (red) MJO events during December–March 1990–2012 in (a) observations and predictions from (b) ACCESS-S1 and (c) POAMA. The plotting convention is as in Fig. 2.

amplitudes of MJO-C events are greater than those of MJO-B. But the predicted mean RMM amplitude for MJO-C quickly decays with lead days, and it becomes comparable to the mean MJO-B amplitude beyond 15-day lead. The small RMM amplitude difference in the ACCESS-S1 forecast compared with observation may arise from the model's inherent biases in representing MJO convection. Similar results are obtained with 8 days earlier start dates in ACCESS-S1 (Fig. S2). The predicted RMM amplitude difference is found to be weakly maintained for the longer lead until the MJO convection center arrives at the MC. It suggests that the model is capable of distinguishing these two types of MJO events well before they encounter the barrier effect of the MC. However, the prominent model biases across the MC play a role in limiting their prediction.

A similar forecast skill assessment is also performed for the POAMA forecast and the results are shown in Fig. S3. The difference in the POAMA prediction skills for the two types of MJO events is greater than that of ACCESS-S1, with skillful MJO-C forecast out to 38 days, whereas only 13 days for MJO-B. This difference is evident in bivariate correlation and ensemble-mean RMSE, likely due to larger start date samples for both the MJO cases in POAMA. Apparently, a greater skill difference with larger samples leads to significant skill differences beyond the 10-day lead. But POAMA is also underdispersive at all lead times as ACCESS-S1 and the model produces a rapid increase in RMSE in the first few lead days, perhaps related to initial atmospheric adjustment to the preferred climatology of the model (Hudson et al. 2011). The potential predictability of both types of MJO events in POAMA is beyond 40 days, but in contrast to ACCESS-S1, potential predictability is significantly higher for MJO-C events. This suggests that the POAMA can indeed predict the difference between MJO-B and MJO-C events beyond any effect coming from difference in initial amplitude. Nevertheless, the RMM amplitudes are underestimated in the POAMA forecast although the difference in amplitude is significant out to lead time 40 days.

The persistently larger RMM amplitude for MJO-C than MJO-B in the observations is maintained in the forecast more so in POAMA than in ACCESS. This naturally raises a question: is the higher prediction skill for the MJO-C events a direct result of them having large amplitude at the initial time? Earlier studies (e.g., Rashid et al. 2011) have shown that MJO prediction skill is strongly dependent on its initial amplitude, with stronger initial amplitude resulting in higher predictive skill. We address this outstanding question by exploring strong and weak MJO cases with similar RMM amplitudes as the MJO-B and MJO-C events over the eastern Indian Ocean in observation and forecast.

c. *Strong versus weak MJO: Observation and forecast*

Figure 4 shows observed and predicted strong and weak MJO propagation in RMM phase-space. For consistency with Fig. 2, we consider MJO events weak if their RMM amplitude at day 0 [|RMM(t = 0)|] over the eastern Indian Ocean (phase 3) is $0.9 < |\text{RMM}(t = 0)| < 1.5$ and strong if $|\text{RMM}(t = 0)| > 1.5$. This provides 40 weak and 33 strong individual MJO cases during DJFM of 1990–2012. The observed strong MJO events over the eastern Indian Ocean are found to dwindle in magnitude across the MC and become weaker in phase 5. In contrast to the MJO-C versus MJO-B events, the strong events are not significantly different from the weak MJO events beyond phase 4. It implies that RMM amplitudes over the eastern equatorial Indian Ocean alone do not determine how MJO events may survive the barrier effect and propagate through the MC.

We have identified start dates of 51 weak and 41 strong MJO events in POAMA and ACCESS-S1 during DJFM 1990–2012. Both models reasonably produce the observed characteristics of the strong and weak MJO events in the forecast. The predicted strong MJO events are marginally slower than the weak ones. Amplitudes of both gradually decrease with lead times. Their differences become less prominent across the MC, suggesting the initial amplitude difference between the strong and weak MJO events is not the key to their propagation across the MC in the forecast as observed.

To assess the possible influence of the initial amplitude on the MJO forecast, the prediction skills of the strong and weak MJO events are examined for ACCESS-S1 (Fig. 5) and

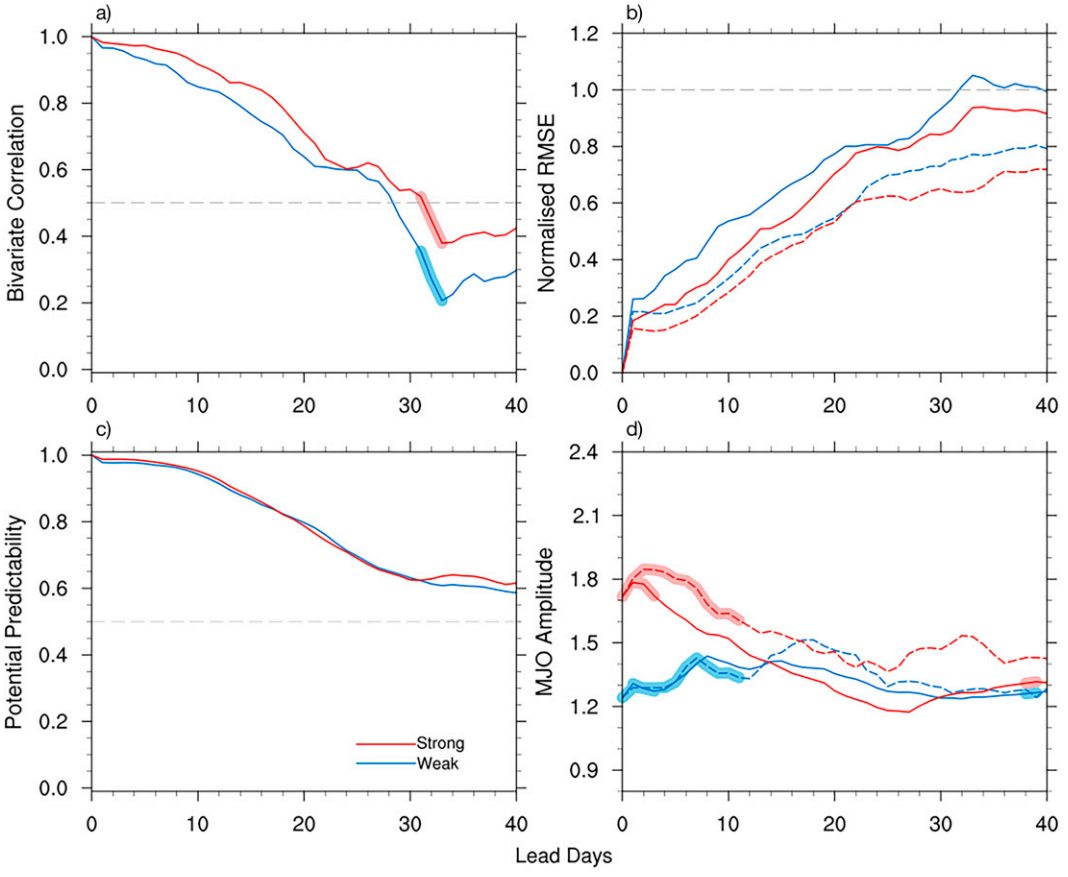

FIG. 5. (a) Bivariate correlation, (b) normalized root-mean-square error (solid curves) and ensemble spread (dashed curves), (c) potential predictability, and (d) mean RMM amplitude from the ACCESS-S1 forecast (solid curves) and observation (dashed curves) for the weak (blue) and strong (red) MJO events for start times around day 0 at phase 3 during December–March 1990–2012. Shading in (a) and (d) indicates where the difference in bivariate correlation and RMM amplitude is significant at the 5% level. The plotting convention is as in Fig. 3.

POAMA (Fig. S4). In contrast to forecast skill difference between MJO-B and MJO-C events, bivariate correlation and ensemble-mean RMSE for strong and weak MJO forecasts are almost similar within the first 30-day lead times in both models. No significant skill difference is noted in either of the models when the forecast is skillful. These two types of MJO events have identical potential predictability beyond 40 days. Stronger initial-mean RMM amplitudes (mean of the ensemble and all the cases) of the strong MJO events decrease with lead times and ACCESS-S1 exaggerates it. POAMA can maintain small-amplitude differences at all lead times, as in the observations. It confirms that the higher prediction skill of MJO-C is not related to their typically stronger amplitudes over the eastern Indian Ocean.

d. Effect of SST anomalies

A plausible reason that MJO-B events do not propagate across the MC islands into the western Pacific is further explored. Motivated by the observational evidence of the persistent subsidence to the east of the MC islands for the MJO-B events (Fig. 1c), we examine the surface conditions for the MJO propagation in observation and forecasts. Figure 6 shows the Hovmöller diagrams of equatorially averaged (10°S–10°N) SST and MSLP anomalies as a function of lead times for both types of MJO events. The observed positive SST and MSLP anomalies show a phase relationship (e.g., Waliser et al. 1999) and systematically propagate eastward in unison from the Indian Ocean to about the date line. The low pressure anomalies at the leading edge of the MJO convection may enhance the moisture convergence induced by the boundary layer friction mechanism, which in turn enhances the instability required for the slow eastward-propagating MJO convection (Wang et al. 2016). Beyond the date line, the positive SST anomalies decrease sharply into negative anomalies, which persist at all the lead times. The negative SST anomalies over the central and eastern Pacific are significantly stronger for MJO-B than for MJO-C, and the colder SST anomalies hydrostatically act to induce high pressure anomalies, thereby suppressing the moisture convergence required for destabilizing the MJO convective phase. We also examine the 120-day high-pass-filtered observed SST anomalies and find that the significant SST difference to the east of the date line is

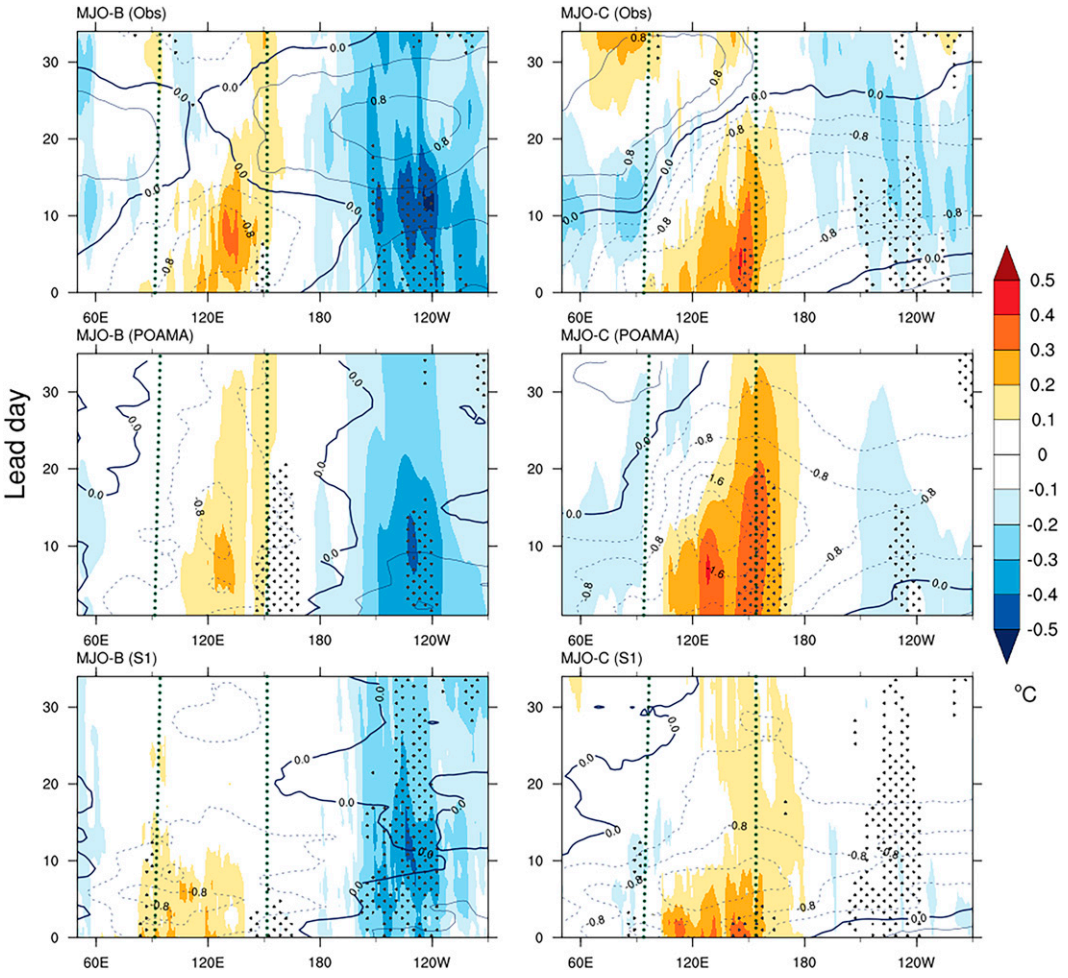

FIG. 6. Equatorially (10°S–10°N) averaged SST (shaded) and MSLP (contours) anomalies for (left) MJO-B and (right) MJO-C events as a function of the lead times during December–March 1990–2012 in (top) ERA-Interim, (middle) POAMA, and (bottom) ACCESS-S1. The significant difference in SST anomalies at the 5% level is stippled. The dark green dotted vertical lines in each panel represent the approximate location of the Maritime Continent islands.

associated with low-frequency variability in the Pacific (Fig. S5). Therefore, the SST difference for MJO-B and MJO-C are not related to intraseasonal variability but are likely linked with the ENSO. The colder SST around the date line restricts the eastward-propagating low pressure anomalies to the west of 150°E and apparently alters the Walker circulation over the Pacific. In contrast, the less cold sea surface of the central Pacific allows MJO-C low pressure anomalies to reach the date line and then they propagate faster as the free Kelvin wave over the cooler ocean.

The stronger negative SST anomalies around the date line for MJO-B are reasonably captured in both models. The eastward propagation of the predicted warm SST anomalies in POAMA are slower and only evident over the eastern Indian Ocean. This problem is even worse in ACCESS-S1, which mostly produces stationary SST anomalies over the warm pool region and overestimates the MC barrier effect. The observed quadrature relationship between SST and MSLP anomalies is reasonably reproduced by POAMA and the subsidence to the east of the date line for MJO-B is captured to a lesser degree. The predicted MJO-B low pressure anomalies are slower than in the observations, consistent with slower eastward propagation of the warm SST anomalies in the forecasts. However, POAMA outperforms ACCESS-S1 in showing eastward-propagating MJO-C low pressure anomalies. ACCESS-S1 produces faster eastward-propagating low pressure anomalies over the warmer SST, suggesting that air–sea interaction related to the MJO over the warm pool region is not properly reproduced in the model. While the subsidence to the east of the date line ascribed a difference in MJO propagation that warrants further investigation, our results indicate that the air–sea interaction may play a critical role in MJO propagation across the MC region.

Finally, we examine the spatial patterns of observed and predicted MJO-B and MJO-C convection over the Indo-Pacific region. The observed OLR and MSLP anomalies at 5-day intervals are shown in Fig. S6, while ACCESS-S1 (POAMA)–predicted anomalies are displayed in Fig. S7 (Fig. S8). Consistent with the results in Fig. 2, the observed MJO-C convection maintains its amplitude as it traverses eastward across the MC islands and subsequently appears over the western Pacific, while MJO-B convection significantly weakens as it crosses the MC islands. A semipersistent positive OLR anomaly to the east of the MC region and extending to the date line, representing sustained subsidence, is apparent for the MJO-B. Together with the negative sustained SST anomalies (please refer to Fig. 6), this subsidence likely acts to stabilize the atmosphere over the western Pacific, thus preventing the emergence of the enhanced MJO convection there for the MJO-B events. It is also evident that both MJO-B and MJO-C convection detour south (and north to a lesser degree) of the MC islands. Thus, rather than the pathway, a difference in the ability to overcome the subsidence to the east of the MC islands is the key to the appearance of the MJO-C convection over the western Pacific.

Both ACCESS-S1 (Fig. S7) and POAMA (Fig. S8) largely capture the different behavior of the convective anomalies to the east of the MC region for MJO-B and MJO-C. Although the predicted MJO-C amplitude over the western Pacific is weaker than observed in both the models (partly due to use of the ensemble mean), the MJO-C convection is evident over the western Pacific at about the 20-day lead. By this time, the predicted MJO-B convection is severely damped over the MC islands.

4. Discussion

In this study, we explore differences in the prediction skills of MJO events that develop in the Indian Ocean and subsequently progress eastward into the western Pacific across the MC region (MJO-C) and those are blocked by the MC region (MJO-B). We use two different ocean–atmosphere coupled forecast systems, a modern high-resolution model (ACCESS-S1), and an older low-resolution model (POAMA). Both the models provide similar results: the predictive skill for the MJO-C events is higher than for the MJO-B events, which is largely consistent with the results from GFDL coupled seamless prediction system (Xiang et al. 2022). The MJO-C events appear over the western Pacific at about the 20-day lead in both ACCESS-S1 and POAMA. The predicted MJO convection exhibits realistic detouring around the MC islands. But the RMM amplitude drops off faster for MJO-B than MJO-C, and the models overestimate the weakening of RMM amplitude for both the MJO cases, a manifestation of the exaggerated barrier effect in models. Although the amplitude of predicted MJO-C over the western Pacific is weaker than observed, models can capture the difference between MJO-B and MJO-C events.

An analysis of the ERA-I dataset reveals that the MJO-B events tend to occur when there is an anomalous sinking motion and higher surface pressures over colder SST in the central Pacific, suggesting that the large-scale environment plays a role in promoting or inhibiting the propagation of the MJO across the MC region. Our analysis also reveals that MJO-C events tend to have a higher initial RMM amplitude when the convective anomaly is developing in the Indian Ocean, even though the MJO-B and MJO-C events exhibit similar initial magnitude convective anomalies around day 0. A significantly greater RMM amplitude of MJO-C suggests that the ability of the MJO convection to overcome the MC island barrier is predetermined. This result is consistent with the notion that the MJO is a coupled circulation–convection disturbance and that the remote circulation anomaly is fundamentally tied to the existence of the MJO. We argue that the greater RMM amplitude for MJO-C is associated with the circulation to the east of the MC region. Although the convective anomalies over the Indian Ocean look similar around day 0, the fundamental differences in large-scale circulation determine the ability of MJO-C events to cross the MC region. The MJO-C events having initially higher RMM amplitude might suggest that the higher skill for the nonblocked events is simply a reflection that higher amplitude MJO events are more predictable (e.g., Rashid et al. 2011; Marshall et al. 2017). But there is clearly more to this explanation because we show that the difference in skill between MJO-B and MJO-C events is much greater than the difference in skill between general MJO events that have a similar RMM amplitude difference. Again, this result points to the underlying role in the background mean state for facilitating and inhibiting propagation across the MC region.

A major caveat to these results is that the potential predictability (i.e., the model's capability to predict itself) is nearly identical for MJO-B and MJO-C events. That is, the models seem to make a similar forecast of the MJO for both MJO events. The insignificant difference in potential predictability indicates that the model prediction skill difference between MJO-B and MJO-C events is unlikely from the barrier effect. So, why is the skill higher for the MJO-C events? The simple answer is that the verification (observed behavior) for the MJO-C events matches the model behavior better than for the MJO-B events. We find comparable prediction skill differences between MJO-B and MJO-C in the statistical VAR model (Fig. S9), which only considers the initial MJO state around day 0 and naturally accounts for persistent eastward propagation. Although the VAR forecast is less skillful than ACCESS-S1 and POAMA, the result supports the difference in MJO behavior across the MC region. A similar explanation has been offered to explain the higher predictive skill of the MJO during easterly phases of the QBO compared to the westerly phase of the MJO (Abhik and Hendon 2019). This study indicates that the dynamical prediction models are less sensitive to the air–sea flux and the role of ocean–atmosphere interaction is fundamental in promoting the MJO propagation across the MC islands into the western Pacific. Improvement in air–sea interaction in the prediction models would be key to advancing the current MJO forecast system. Nonetheless, our results are still of practical importance because the models do faithfully maintain higher amplitudes for a longer duration for the nonblocked events, suggesting there is useful information provided by the forecast as to whether the MJO

convection will sustain until it reaches the western Pacific. Something about systematic error might make differences less prominent than they are in reality. Future assessment with more start dates in the multimodel S2S forecast framework (Vitart et al. 2017) may reduce the model uncertainty and will lead to advancing our understanding of the interaction between large-scale circulation and MJO convection over the MC region.

Acknowledgments. This work is funded by the Northern Australia Climate Program (NACP) and Pacific Marine Environmental Laboratory (PMEL) Contribution 5338. We thank the BOM Seasonal Prediction team for making the hindcast data available. The insightful comments from three anonymous reviewers and the editor Daehyun Kim greatly helped to improve the earlier version of the manuscript. We also thank Matthew C. Wheeler, Andrew Marshall, and S. Sharmila for providing constructive suggestions during the internal review process. This research was undertaken with the assistance of resources and services from the National Computational Infrastructure (NCI), which is supported by the Australian Government. The analyses were performed using the NCAR Command Language: https://doi.org/10.5065/D6WD3XH5.

Data availability statement. Daily interpolated OLR data were obtained from NOAA/ESRL PSD, Boulder, Colorado: https://www.esrl.noaa.gov/psd/data/gridded/data.interp_OLR.html. NCEP Reanalysis data were provided by the NOAA/OAR/ESRL PSL, Boulder, Colorado, from https://psl.noaa.gov/data/gridded/data.ncep.reanalysis2.html. ERA-Interim data were downloaded from ECMWF: http//apps.ecmwf.int/datasets/data/interim_full_daily. Observed RMM index was obtained from http://www.bom.gov.au/climate/mjo/graphics/rmm.74toRealtime.txt. The ACCESS-S1 and POAMA hindcast datasets are available from the corresponding author upon reasonable request.

REFERENCES

Abhik, S., and H. H. Hendon, 2019: Influence of the QBO on the MJO during coupled model multiweek forecasts. *Geophys. Res. Lett.*, **46**, 9213–9221, https://doi.org/10.1029/2019GL083152.

Ahn, M.-S., and Coauthors, 2020: MJO propagation across the Maritime Continent: Are CMIP6 models better than CMIP5 models? *Geophys. Res. Lett.*, **47**, e2020GL087250, https://doi.org/10.1029/2020GL087250.

Baranowski, D. B., D. E. Waliser, X. Jiang, J. A. Ridout, and M. K. Flatau, 2019: Contemporary GCM fidelity in representing the diurnal cycle of precipitation over the Maritime Continent. *J. Geophys. Res. Atmos.*, **124**, 747–769, https://doi.org/10.1029/2018JD029474.

Blockley, E. W., and Coauthors, 2014: Recent development of the Met Office operational ocean forecasting system: An overview and assessment of the new global FOAM forecasts. *Geosci. Model Dev.*, **7**, 2613–2638, https://doi.org/10.5194/gmd-7-2613-2014.

Bretherton, C. S., M. Widmann, V. P. Dymnikov, J. M. Wallace, and I. Bladé, 1999: The effective number of spatial degrees of freedom of a time-varying field. *J. Climate*, **12**, 1990–2009, https://doi.org/10.1175/1520-0442(1999)012<1990:TENOSD>2.0.CO;2.

Chen, G., and B. Wang, 2018: Effects of enhanced front walker cell on the eastward propagation of the MJO. *J. Climate*, **31**, 7719–7738, https://doi.org/10.1175/JCLI-D-17-0383.1.

Dee, D. P., and Coauthors, 2011: The ERA-interim reanalysis: Configuration and performance of the data assimilation system. *Quart. J. Roy. Meteor. Soc.*, **137**, 553–597, https://doi.org/10.1002/qj.828.

DeMott, C. A., B. O. Wolding, E. D. Maloney, and D. A. Randall, 2018: Atmospheric mechanisms for MJO decay over the Maritime Continent. *J. Geophys. Res. Atmos.*, **123**, 5188–5204, https://doi.org/10.1029/2017JD026979.

Feng, J., T. Li, and W. Zhu, 2015: Propagating and nonpropagating MJO events over Maritime Continent. *J. Climate*, **28**, 8430–8449, https://doi.org/10.1175/JCLI-D-15-0085.1.

Hagos, S. M., C. Zhang, Z. Feng, C. D. Burleyson, C. De Mott, B. Kerns, J. J. Benedict, and M. N. Martini, 2016: The impact of the diurnal cycle on the propagation of Madden-Julian oscillation convection across the Maritime Continent. *J. Adv. Model. Earth Syst.*, **8**, 1552–1564, https://doi.org/10.1002/2016MS000725.

Hendon, H. H., and M. L. Salby, 1994: The life cycle of the Madden–Julian oscillation. *J. Atmos. Sci.*, **51**, 2225–2237, https://doi.org/10.1175/1520-0469(1994)051<2225:TLCOTM>2.0.CO;2.

Houze, R. A., S. G. Geotis, F. D. Marks, and A. K. West, 1981: Winter monsoon convection in the vicinity of North Borneo. Part I: Structure and time variation of the clouds and precipitation. *Mon. Wea. Rev.*, **109**, 1595–1614, https://doi.org/10.1175/1520-0493(1981)109<1595:WMCITV>2.0.CO;2.

Hsu, H.-H., and M.-Y. Lee, 2005: Topographic effects on the eastward propagation and initiation of the Madden–Julian oscillation. *J. Climate*, **18**, 795–809, https://doi.org/10.1175/JCLI-3292.1.

Hu, Q., and D. A. Randall, 1994: Low-frequency oscillations in radiative-convective systems. *J. Atmos. Sci.*, **51**, 1089–1099, https://doi.org/10.1175/1520-0469(1994)051<1089:LFOIRC>2.0.CO;2.

——, and ——, 1995: Low-frequency oscillations in radiative-convective systems. Part II: An idealized model. *J. Atmos. Sci.*, **52**, 478–490, https://doi.org/10.1175/1520-0469(1995)052<0478:LFOIRC>2.0.CO;2.

Hudson, D., O. Alves, H. H. Hendon, and G. Wang, 2011: The impact of atmospheric initialisation on seasonal prediction of tropical pacific SST. *Climate Dyn.*, **36**, 1155–1171, https://doi.org/10.1007/s00382-010-0763-9.

——, A. G. Marshall, Y. Yin, O. Alves, and H. H. Hendon, 2013: Improving intraseasonal prediction with a new ensemble generation strategy. *Mon. Wea. Rev.*, **141**, 4429–4449, https://doi.org/10.1175/MWR-D-13-00059.1.

——, and Coauthors, 2017: ACCESS-S1: The new bureau of meteorology multi-week to seasonal prediction system. *J. South. Hemisphere Earth Syst. Sci.*, **67**, 132–159, https://doi.org/10.1071/ES17009.

Inness, P. M., and J. M. Slingo, 2006: The interaction of the Madden–Julian oscillation with the Maritime Continent in a GCM. *Quart. J. Roy. Meteor. Soc.*, **132**, 1645–1667, https://doi.org/10.1256/qj.05.102.

Jiang, X., 2017: Key processes for the eastward propagation of the Madden–Julian oscillation based on multimodel simulations. *J. Geophys. Res. Atmos.*, **122**, 755–770, https://doi.org/10.1002/2016JD025955.

——, and Coauthors, 2015: Vertical structure and physical processes of the Madden–Julian oscillation: Exploring key model physics in climate simulations. *J. Geophys. Res. Atmos.*, **120**, 4718–4748, https://doi.org/10.1002/2014JD022375.

Johnson, R. H., T. M. Rickenbach, S. A. Rutledge, P. E. Ciesielski, and W. H. Schubert, 1999: Trimodal characteristics of tropical convection. *J. Climate*, **12**, 2397–2418, https://doi.org/10.1175/1520-0442(1999)012<2397:TCOTC>2.0.CO;2.

Kalnay, E., and Coauthors, 1996: The NCEP/NCAR 40-Year Reanalysis Project. *Bull. Amer. Meteor. Soc.*, **77**, 437–472, https://doi.org/10.1175/1520-0477(1996)077<0437:TNYRP>2.0.CO;2.

Kiladis, G. N., J. Dias, K. H. Straub, M. C. Wheeler, S. N. Tulich, K. Kikuchi, K. M. Weickmann, and M. J. Ventrice, 2014: A comparison of OLR and circulation-based indices for tracking the MJO. *Mon. Wea. Rev.*, **142**, 1697–1715, https://doi.org/10.1175/MWR-D-13-00301.1.

Kim, D., J.-S. Kug, and A. H. Sobel, 2014: Propagating versus nonpropagating Madden–Julian oscillation events. *J. Climate*, **27**, 111–125, https://doi.org/10.1175/JCLI-D-13-00084.1.

Kim, H.-M., D. Kim, F. Vitart, V. E. Toma, J.-S. Kug, and P. J. Webster, 2016: MJO propagation across the Maritime Continent in the ECMWF ensemble prediction system. *J. Climate*, **29**, 3973–3988, https://doi.org/10.1175/JCLI-D-15-0862.1.

Liebmann, B., and C. A. Smith, 1996: Description of a complete (interpolated) outgoing longwave radiation dataset. *Bull. Amer. Meteor. Soc.*, **77**, 1275–1277, https://doi.org/10.1175/1520-0477-77.6.1274.

Ling, J., P. Bauer, P. Bechtold, A. Beljaars, R. Forbes, F. Vitart, M. Ulate, and C. Zhang, 2014: Global versus local MJO forecast skill of the ECMWF model during DYNAMO. *Mon. Wea. Rev.*, **142**, 2228–2247, https://doi.org/10.1175/MWR-D-13-00292.1.

——, C. Zhang, R. Joyce, P.-P. Xie, and G. Chen, 2019: Possible role of the diurnal cycle in land convection in the barrier effect on the MJO by the Maritime Continent. *Geophys. Res. Lett.*, **46**, 3001–3011, https://doi.org/10.1029/2019GL081962.

MacLachlan, C., and Coauthors, 2015: Global seasonal forecast system version 5 (GloSea5): A high-resolution seasonal forecast system. *Quart. J. Roy. Meteor. Soc.*, **141**, 1072–1084, https://doi.org/10.1002/qj.2396.

Madden, R. A., and P. R. Julian, 1971: Detection of a 40–50 day oscillation in the zonal wind in the tropical pacific. *J. Atmos. Sci.*, **28**, 702–708, https://doi.org/10.1175/1520-0469(1971)028<0702:DOADOI>2.0.CO;2.

——, and ——, 1972: Description of global-scale circulation cells in the tropics with a 40–50 day period. *J. Atmos. Sci.*, **29**, 1109–1123, https://doi.org/10.1175/1520-0469(1972)029<1109:DOGSCC>2.0.CO;2.

Maharaj, E. A., and M. C. Wheeler, 2005: Forecasting an index of the Madden-Julian oscillation. *Int. J. Climatol.*, **25**, 1611–1618, https://doi.org/10.1002/joc.1206.

Majda, A. J., and Q. Yang, 2016: A multiscale model for the intraseasonal impact of the diurnal cycle over the Maritime Continent on the Madden–Julian oscillation. *J. Atmos. Sci.*, **73**, 579–604, https://doi.org/10.1175/JAS-D-15-0158.1.

Maloney, E. D., and A. H. Sobel, 2004: Surface fluxes and ocean coupling in the tropical intraseasonal oscillation. *J. Climate*, **17**, 4368–4386, https://doi.org/10.1175/JCLI-3212.1.

Marshall, A. G., D. Hudson, M. C. Wheeler, H. H. Hendon, and O. Alves, 2011: Assessing the simulation and prediction of rainfall associated with the MJO in the POAMA seasonal forecast system. *Climate Dyn.*, **37**, 2129–2141, https://doi.org/10.1007/s00382-010-0948-2.

——, H. H. Hendon, S.-W. Son, and Y. Lim, 2017: Impact of the quasi-biennial oscillation on predictability of the Madden–Julian oscillation. *Climate Dyn.*, **49**, 1365–1377, https://doi.org/10.1007/s00382-016-3392-0.

——, and ——, 2019: Multi-week prediction of the Madden–Julian oscillation with ACCESS-S1. *Climate Dyn.*, **52**, 2513–2528, https://doi.org/10.1007/s00382-018-4272-6.

Megann, A., and Coauthors, 2014: GO5.0: The joint NERC–Met Office NEMO global ocean model for use in coupled and forced applications. *Geosci. Model Dev.*, **7**, 1069–1092, https://doi.org/10.5194/gmd-7-1069-2014.

Mori, S., and Coauthors, 2004: Diurnal land–sea rainfall peak migration over Sumatera Island, Indonesian Maritime Continent, observed by TRMM satellite and intensive rawinsonde soundings. *Mon. Wea. Rev.*, **132**, 2021–2039, https://doi.org/10.1175/1520-0493(2004)132<2021:DLRPMO>2.0.CO;2.

Murphy, A. H., and E. S. Epstein, 1989: Skill scores and correlation coefficients in model verification. *Mon. Wea. Rev.*, **117**, 572–582, https://doi.org/10.1175/1520-0493(1989)117<0572:SSACCI>2.0.CO;2.

Neale, R., and J. Slingo, 2003: The Maritime Continent and its role in the global climate: A GCM study. *J. Climate*, **16**, 834–848, https://doi.org/10.1175/1520-0442(2003)016<0834:TMCAIR>2.0.CO;2.

Peatman, S. C., A. J. Matthews, and D. P. Stevens, 2014: Propagation of the Madden–Julian oscillation through the Maritime Continent and scale interaction with the diurnal cycle of precipitation. *Quart. J. Roy. Meteor. Soc.*, **140**, 814–825, https://doi.org/10.1002/qj.2161.

Rashid, H. A., H. H. Hendon, M. C. Wheeler, and O. Alves, 2011: Prediction of the Madden–Julian oscillation with the POAMA dynamical prediction system. *Climate Dyn.*, **36**, 649–661, https://doi.org/10.1007/s00382-010-0754-x.

Rowe, A. K., and R. A. Houze Jr., 2015: Cloud organization and growth during the transition from suppressed to active MJO conditions. *J. Geophys. Res. Atmos.*, **120**, 10 324–10 350, https://doi.org/10.1002/2014JD022948.

Rowell, D. P., 1998: Assessing potential seasonal predictability with an ensemble of multidecadal GCM simulations. *J. Climate*, **11**, 109–120, https://doi.org/10.1175/1520-0442(1998)011<0109:APSPWA>2.0.CO;2.

Ruppert, J. H., Jr., and R. H. Johnson, 2015: Diurnally modulated cumulus moistening in the preonset stage of the Madden–Julian oscillation during DYNAMO. *J. Atmos. Sci.*, **72**, 1622–1647, https://doi.org/10.1175/JAS-D-14-0218.1.

Sobel, A. H., and E. D. Maloney, 2013: Moisture modes and the eastward propagation of the MJO. *J. Atmos. Sci.*, **70**, 187–192, https://doi.org/10.1175/JAS-D-12-0189.1.

——, ——, G. Bellon, and D. M. Frierson, 2010: Surface fluxes and tropical intraseasonal variability: A reassessment. *J. Adv. Model. Earth Syst.*, **2**, 2, https://doi.org/10.3894/JAMES.2010.2.2.

——, S. Wang, and D. Kim, 2014: Moist static energy budget of the MJO during DYNAMO. *J. Atmos. Sci.*, **71**, 4276–4291, https://doi.org/10.1175/JAS-D-14-0052.1.

Tan, H., P. Ray, B. S. Barrett, M. Tewari, and M. W. Moncrieff, 2020: Role of topography on the MJO in the Maritime Continent: A numerical case study. *Climate Dyn.*, **55**, 295–314, https://doi.org/10.1007/s00382-018-4275-3.

Vitart, F., and F. Molteni, 2010: Simulation of the Madden–Julian oscillation and its teleconnections in the ECMWF forecast

system. *Quart. J. Roy. Meteor. Soc.*, **136**, 842–855, https://doi.org/10.1002/qj.623.

——, and Coauthors, 2017: The Subseasonal to Seasonal (S2S) prediction project database. *Bull. Amer. Meteor. Soc.*, **98**, 163–173, https://doi.org/10.1175/BAMS-D-16-0017.1.

Waliser, D. E., K. M. Lau, and J.-H. Kim, 1999: The influence of coupled sea surface temperatures on the Madden–Julian oscillation: A model perturbation experiment. *J. Atmos. Sci.*, **56**, 333–358, https://doi.org/10.1175/1520-0469(1999)056<0333:TIOCSS>2.0.CO;2.

——, ——, W. Stern, and C. Jones, 2003: Potential predictability of the Madden–Julian oscillation. *Bull. Amer. Meteor. Soc.*, **84**, 33–50, https://doi.org/10.1175/BAMS-84-1-33.

Walters, D., and Coauthors, 2017: The Met Office Unified Model Global Atmosphere 6.0/6.1 and JULES Global Land 6.0/6.1 configurations. *Geosci. Model Dev.*, **10**, 1487–1520, https://doi.org/10.5194/gmd-10-1487-2017.

Wang, B., F. Liu, and G. Chen, 2016: A trio-interaction theory for Madden–Julian oscillation. *Geosci. Lett.*, **3**, 34, https://doi.org/10.1186/s40562-016-0066-z.

——, G. Chen, and F. Liu, 2019: Diversity of the Madden-Julian oscillation. *Sci. Adv.*, **5**, eaax0220, https://doi.org/10.1126/sciadv.aax0220.

Weaver, S. J., W. Wang, M. Chen, and A. Kumar, 2011: Representation of MJO variability in the NCEP climate forecast system. *J. Climate*, **24**, 4676–4694, https://doi.org/10.1175/2011JCLI4188.1.

Weisheimer, A., T. N. Palmer, and F. J. Doblas-Reyes, 2011: Assessment of representations of model uncertainty in monthly and seasonal forecast ensembles. *Geophys. Res. Lett.*, **38**, L16703, https://doi.org/10.1029/2011GL048123.

Wheeler, M. C., and H. H. Hendon, 2004: An all-season real-time multivariate MJO index: Development of an index for monitoring and prediction. *Mon. Wea. Rev.*, **132**, 1917–1932, https://doi.org/10.1175/1520-0493(2004)132<1917:AARMMI>2.0.CO;2.

Wu, C.-H., and H.-H. Hsu, 2009: Topographic influence on the MJO in the Maritime Continent. *J. Climate*, **22**, 5433–5448, https://doi.org/10.1175/2009JCLI2825.1.

Xiang, B., and Coauthors, 2022: S2S prediction in GFDL SPEAR: MJO diversity and teleconnections. *Bull. Amer. Meteor. Soc.*, **103**, E463–E484, https://doi.org/10.1175/BAMS-D-21-0124.1.

Yamanaka, M. D., 2016: Physical climatology of Indonesian Maritime Continent: An outline to comprehend observational studies. *Atmos. Res.*, **178–179**, 231–259, https://doi.org/10.1016/j.atmosres.2016.03.017.

Yin, Y., O. Alves, and P. R. Oke, 2011: An ensemble ocean data assimilation system for seasonal prediction. *Mon. Wea. Rev.*, **139**, 786–808, https://doi.org/10.1175/2010MWR3419.1.

Zhang, C., and J. Ling, 2017: Barrier effect of the Indo-Pacific Maritime Continent on the MJO: Perspectives from tracking MJO precipitation. *J. Climate*, **30**, 3439–3459, https://doi.org/10.1175/JCLI-D-16-0614.1.